

# Implications of non-electrochemical reaction steps on the oxygen evolution reaction: Oxygen dimer formation on perovskite oxide and oxynitride surfaces

Nathalie Vonrüti,<sup>†</sup> Reshma Rao,<sup>‡</sup> Livia Giordano,<sup>‡</sup> Yang Shao-Horn,<sup>‡</sup> and Ulrich Aschauer<sup>\*,†</sup>

<sup>†</sup>*Department of Chemistry, Biochemistry and Pharmaceutical Science, University of Bern, Freiestrasse 3, CH-3012 Bern, Switzerland*

<sup>‡</sup>*Research Laboratory of Electronics, Massachusetts Institute of Technology, Cambridge, Massachusetts 02139, USA*

E-mail: ulrich.aschauer@unibe.ch

## Abstract

According to conventional understanding, the oxygen evolution reaction on metal-oxide surfaces involves four proton-coupled electron transfer steps with  $^*\text{OH}$ ,  $^*\text{O}$  and  $^*\text{OOH}$  reaction intermediates. Recently, several alternative reaction mechanisms with lower overpotentials were proposed for highly active catalysts. While for such reaction mechanisms additional intermediates leading to non-electrochemical reaction steps could be considered, they are usually neglected when investigating the thermodynamic overpotential of such mechanisms. We show here that this is a valid approximation for endothermic non-electrochemical steps, which only affect the kinetics, while exothermic non-electrochemical steps can also affect the thermodynamic overpotential. We

show this based on density functional theory calculations for one of those proposed mechanisms on surfaces of different perovskite oxides and oxynitrides. We find that for weakly binding surfaces the \*O adsorbate spontaneously adopts a bidentate bridged dimer structure in a non-electrochemical step with an energy gain in excess of 1 eV. This decrease in free energy needs to be compensated by an equivalent increase in magnitude of the electrochemical steps, which can affect the thermodynamic overpotential. This change may result in reaction mechanisms without non-electrochemical steps having smaller thermodynamic overpotentials and thus be more favorable.

## Keywords

OER, alternative mechanisms, oxygen dimer, lattice oxygen vacancy, DFT

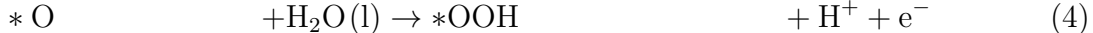
## Introduction

(Photo)electrochemical water splitting is a promising route to convert solar or electrical energy into chemical energy.<sup>1-3</sup> The overall water splitting reaction is endothermic and requires 4.92 eV ( $\Delta$ ) to split two water molecules into an oxygen and two hydrogen molecules,  $\Delta$  being provided for example by electrical or solar energy:



Due to its complexity, the oxygen evolution reaction (OER) is the kinetic bottleneck of the overall water-splitting reaction<sup>4</sup> and a detailed mechanistic knowledge is crucial for the development of efficient molecular<sup>5-7</sup> and heterogeneous catalysts.<sup>8-12</sup> According to conventional understanding, the OER mechanism **M1** on metal-oxide surfaces involves four proton-coupled electron transfer steps on metal-ion centers with OH, O and OOH reaction

intermediates, \* indicating the active metal site (see also Fig. 1a):



OER mechanism **M1** has been studied extensively and was shown to have a relatively large theoretical overpotential of 0.37 V due to the universal scaling relation between the adsorption energies of the OOH and OH reaction intermediates on metal and transition-metal sites.<sup>13,14</sup> While for metal oxides such as rutiles ( $\text{MO}_2$ ) coordinately undersaturated transition-metal sites were considered as active sites,<sup>15-17</sup> for  $\text{ABO}_3$  perovskite oxides mostly the B site was considered as the active site.<sup>18,19</sup>

A computational analysis of the OER is often simplified by only considering the \*OH, \*O and \*OOH reaction intermediates appearing in the electrochemical steps shown in equations 2-5.<sup>14,20-22</sup> Nevertheless, additional reaction intermediates could be considered that lead to non-electrochemical reaction steps. For simplicity we will refer to these as *chemical steps* in the following. We also note that we define, in accordance with concerted proton-electron transfer, a chemical step as one for which no proton transfer and thus also no electron transfer with a reservoir exists. To relax this assumption and to allow sequential proton and electron transfer, potentially in separate steps, it would be highly desirable to find a DFT-based marker for chemical vs. electrochemical steps, which will require accounting for the counter electrode in the calculation, likely implicitly,<sup>23</sup> as well as the explicit electrolyte. As an example for such additional chemical steps, the reaction in equation 5 can be considered to consist of two steps, an electrochemical and a chemical step, that proceed via the reaction

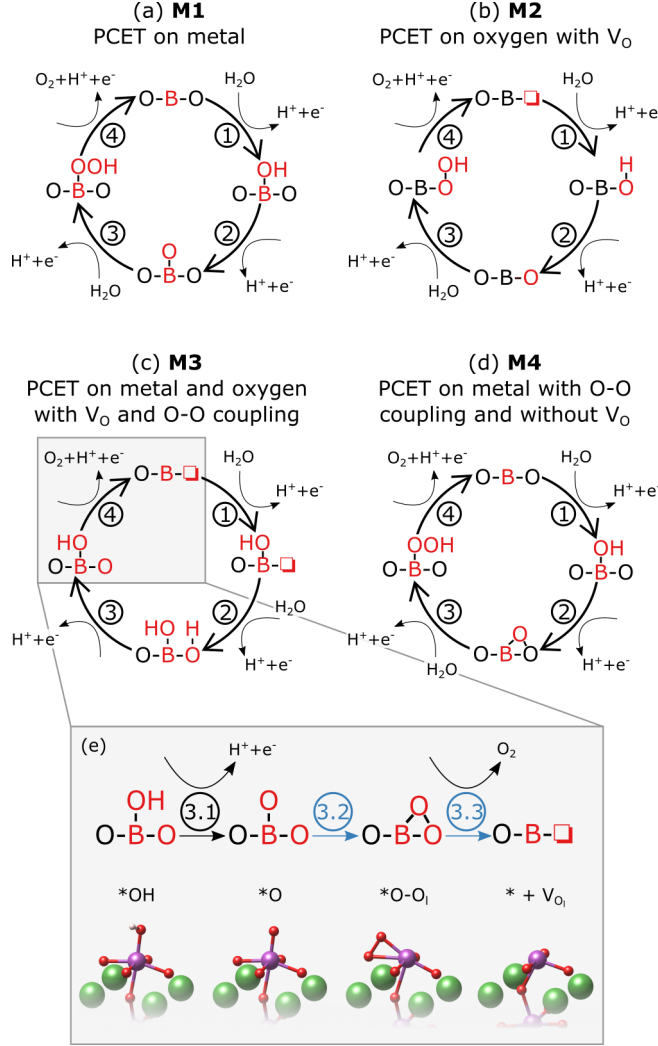


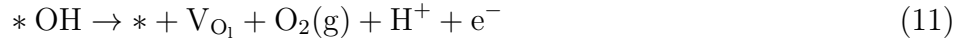
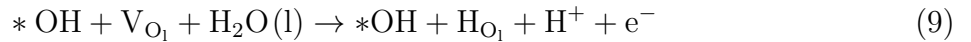
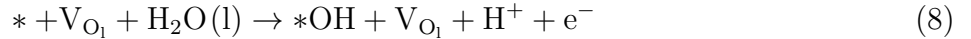
Figure 1: Electrochemical steps of different reaction mechanisms considered in this study (a) **M1** conventional reaction mechanism, (b) **M2** conventional reaction mechanism on a lattice oxygen, (c) **M3** alternative lattice oxygen mechanism, (d) **M4** dimer formation within the conventional reaction mechanism, (e) some of the possible non-electrochemical steps involved in **M3** along with corresponding atomic structures of the additional reaction intermediates. Electrochemical steps are shown by black and purely chemical steps by blue arrows. While schematics are shown for a B site geometry, A sites were also investigated as active sites in this work. Color code: A-site=green, B-site=purple, O=red.

intermediate  $^*\text{OO}$ , a dioxygen bound to the active site:<sup>24</sup>



The usually good agreement in the activity trend (not in actual overpotentials) between experiment and computation, however, seems to justify neglecting this chemical step in a computational analysis of **M1**.

Recently, alternative reaction mechanisms with lower thermodynamic overpotentials and supposedly higher activities have been proposed, in particular for less stable catalytic materials, where surface defects can play a role.<sup>25</sup> These mechanism may therefore be especially relevant on mixed-anion materials, such as oxynitrides, that are inherently less stable than their pure oxide counterparts.<sup>26</sup> Many of these newly proposed mechanisms involve so-called lattice oxygen ( $\text{O}_l$ ), where oxygen ions of the catalyst act as active site (such as mechanism **M2** in Fig. 1b).<sup>27</sup> Involving  $\text{O}_l$  increases the number of active sites and/or leads to reaction mechanisms with smaller theoretical overpotentials than **M1** (such as mechanism **M3** in Fig. 1c).<sup>25,28,29</sup> Mechanism **M3** differs in most of its steps from the conventional mechanism **M1**:



where  $^*$  is the active metal site,  $\text{H}_{\text{O}_l}$  denotes a hydrogen atom which forms a chemical bond with a lattice oxygen and  $\text{V}_{\text{O}_l}$  is a lattice oxygen vacancy. In equation 9, the water molecule is oxidized to OH, which then fills the  $\text{V}_{\text{O}_l}$ . For many of these alternative mechanisms, additional reaction intermediates can be considered during computational analysis<sup>25,27</sup> leading

not only to electrochemical but also chemical reaction steps. As such, the reaction step shown in equation 11 could contain multiple chemical steps if additional intermediates are considered as shown in Fig. 1e. We assume here that after the electrochemical deprotonation of  $^*\text{OH}$ , two chemical steps lead to dimer formation and finally  $\text{O}_2$  evolution. While it would be possible to consider different or additional chemical steps,<sup>29</sup> these intermediates are not always easy to stabilize in DFT and, as we will show later, will not affect our conclusions. In particular, oxygen dimer formation (step 3.2 in Fig. 1e) was shown to be exothermic in excess of 1 eV for some materials.<sup>29</sup> We note here that mechanism **M1** could also be considered to contain a chemical step, if the  $^*\text{O}$  adsorbate does not remain upright but also forms a dimer as shown in mechanism **M4**. The effect of such chemical steps on the electrochemical steps of **M1** was, however, not previously quantified.

In the present study we will assess trends for the occurrence and magnitude of chemical steps, as well as their effect on the electrochemical steps and therefore the activity of the overall reaction mechanism. As a starting point we use a database containing density-functional theory (DFT) calculation of the OER on defective perovskite oxides ( $\text{ABO}_3$ ) and oxynitride ( $\text{ABO}_2\text{N}$ ) surfaces ( $\text{LaTiO}_2\text{N}$ ,  $\text{SrRuO}_3$  and  $\text{SrTiO}_3$ ), which we obtained in a previous study.<sup>30</sup> While  $\text{SrRuO}_3$  is known to be a viable electrocatalyst,  $\text{LaTiO}_2\text{N}$  and  $\text{SrTiO}_3$  can act as photocatalysts, by virtue of their band gaps that lie in the visible and UV range respectively. Less stable materials with many defects (in this case atomic vacancies) are well suited to analyze the influence of purely chemical reaction steps since alternative reaction mechanisms were proposed to preferentially occur on such materials.<sup>25</sup> We observe that the formation of an oxygen dimer as a result of a chemical step is likely for many of these surfaces and therefore investigate part of reaction mechanism **M3** (see Fig. 1c and e) that contains such a dimer formation. We find that dimer formation, that was previously shown to be exothermic in excess of 2 eV for example for  $\text{LaCuO}_3$ ,<sup>29</sup> can render reaction mechanism **M3** less favorable than other mechanisms. These findings are supported by calculations on surfaces of different non-defective perovskite oxides. The insight of exothermic chemical steps

potentially increasing the thermodynamic overpotential, is general and not limited to dimer formation or lattice oxygen participation. This demonstrates that chemical steps should be included when analyzing reaction mechanisms other than the conventional mechanism **M1** for which we confirm chemical reaction steps to be negligible.

## Computational methods

We analyze binding energies of reaction intermediates and the resulting overall catalytic activity of different reaction mechanisms based on two databases. The first database, obtained in a previous study,<sup>30</sup> contains data for LaTiO<sub>2</sub>N, SrTiO<sub>3</sub> and SrRuO<sub>3</sub> (001) surfaces, considering 778 symmetrically distinct reaction sites on defective surfaces. Surfaces in this database are both A and B terminated and contain between zero and four A-site, B-site or nitrogen vacancies in the topmost atomic layer, a perfect atomic layer containing four A or B sites (see supporting information (SI) Fig. S1 for sample surface structures). Surfaces with preexisting oxygen vacancies were not considered as they are unlikely under oxidising OER conditions,<sup>31</sup> but oxygen vacancies may still form during a reaction mechanism. Surfaces are either not covered with adsorbates or fully covered with OH or O adsorbates in the bridge or top position (see SI section S1). Despite the large amount of data, this database has the drawback of a significant, vacancy-induced structural flexibility, that makes it difficult to extract clear trends and to fit descriptors (see SI section S2). Therefore, in a second database we analyze adsorption energies for A and B terminated surfaces of eight different perovskite oxides and oxynitrides, without any surface vacancies. From now on, we will refer to the database taken from our previous work<sup>30</sup> as database 1a and a database extended using the same computational setup but with additional reaction-intermediate starting positions (see SI section S3) as database 1b. In both of these databases, we excluded cases where the OOH intermediate was not stable and spontaneously decayed to more than one adsorbate, for example by hydrogen or OH transfer, leading to -OO and -OH adsorbates.

While reaction mechanisms involving such split adsorbates are possible,<sup>8,15,32–34</sup> we excluded them from our analysis to reduce the complexity. The database containing the defect-free surfaces is referred to as database 2.

For both databases we compute total energies via density functional theory as implemented in Quantum ESPRESSO<sup>35,36</sup> using the PBE+ $U$ <sup>37,38</sup> density functional. While the computational setup for database 1 (1a and 1b) can be found in our previous study<sup>30</sup> the computational setup for the database 2 as well as an overview of the differences between the two databases can be found in SI section S3. In summary, calculations in database 1 were performed with a kinetic energy cutoff of 40 Ry combined with 320 Ry for the augmented density for LaTiO<sub>2</sub>N and SrTiO<sub>3</sub>, while a higher cutoff of 50 Ry combined with 500 Ry for the augmented density was used for SrRuO<sub>3</sub>. A Hubbard  $U$ <sup>38</sup> correction of 3 eV was applied to the Ti 3*d* states and reciprocal space of our  $2 \times 2$  surface slabs was sampled with  $4 \times 4 \times 1$  and  $6 \times 6 \times 1$  meshes for LaTiO<sub>2</sub>N/SrTiO<sub>3</sub> and SrRuO<sub>3</sub> respectively. For calculations in database 2 we derived linear response<sup>39</sup> Hubbard  $U$  parameters (see SI Section S3 for specific  $U$  values). Obtaining convergence of these  $U$  parameters required a larger cutoff of 70 Ry combined with 700 Ry for the augmented density as well as denser  $6 \times 6 \times 6$  k-meshes for bulk and consequently  $6 \times 6 \times 1$  for surface calculations. All surfaces were constructed as periodic vacuum slabs with a minimum 10 Å vacuum gap and a dipole correction.<sup>40</sup>

We estimate the catalytic activity of a specific reaction site by the largest electrochemical step in the OER free energy profile

$$\Delta G^{\text{OER}} = \max[\Delta G_i^0] \quad (12)$$

$\Delta G_i^0$  being the change in free energy of the electrochemical OER step  $i$ . For OH or O covered surfaces, the order of steps (Eq. 2 to 5) is modified such that the first step starts with the preexisting adsorbate.<sup>20,21</sup> We then derive the thermodynamic overpotential as

$$\eta^{\text{OER}} = \Delta G^{\text{OER}}/e - 1.23 \text{ V} \quad (13)$$



where 1.23 V is the equilibrium potential. The reaction steps ( $\Delta G_i^0$ ) were calculated from differences in adsorption energies of the various intermediates ( $\Delta G_{\text{OH}}$ ,  $\Delta G_{\text{O}}$ ,  $\Delta G_{\text{OOH}}$ ). Since the theoretical overpotential does not depend on the pH or the potential<sup>13</sup> we calculated adsorption energies at standard conditions (pH=0,  $T = 298.15$  K) and  $U = 0$  V using the computational hydrogen electrode,<sup>41</sup> where the energy of a proton and an electron equals half the energy of a hydrogen molecule. All adsorption energies ( $G_{\text{ads}}$ ) are defined with respect to water and hydrogen

$$\Delta G_{\text{ads}} = G_{\text{ads+slab}} - G_{\text{slab}} - nG_{\text{H}_2\text{O}} - mG_{\text{H}_2} \quad (14)$$

with  $n$  and  $m$  stoichiometry coefficients that preserve the number of atoms on both sides of the respective reaction. Free energy differences ( $\Delta G$ ) include changes in zero-point energy (ZPE) and entropy ( $S$ ) that were taken from elsewhere<sup>21,29</sup> since ZPE values show little site and material dependence (see also SI section S4) and since a full evaluation for all sites on our defective surfaces would be prohibitive. We further calculate the energy (subtracting the free energy contributions) of the oxygen molecule ( $E_{\text{O}_2}$ ) as

$$E_{\text{O}_2} = 4.92 - 2E_{\text{H}_2} + 2E_{\text{H}_2\text{O}} - (\Delta\text{ZPE} - T\Delta S)_{2\text{H}_2\text{O} \rightarrow 2\text{H}_2 + \text{O}_2} \quad (15)$$

since the generalized gradient approximation (GGA) is known to overestimate the  $\text{O}_2$  binding energy and using a DFT calculated  $\text{O}_2$  total energy can lead to large and functional dependent errors.<sup>42</sup> Here  $E_{\text{H}_2}$  and  $E_{\text{H}_2\text{O}}$  stand for the DFT energies of hydrogen and water, respectively. We neglect the effect of integrated heat capacities of molecules between the DFT temperature of 0 K and  $T = 298.15$  K, which is justified by the similar magnitude of this quantity for the different involved molecules that largely leads to cancellation of this contribution.<sup>43</sup>

For the conventional reaction mechanism **M1** the overpotential is usually determined by

either  $\Delta G_2^0 = \Delta G_O - \Delta G_{OH}$  or  $\Delta G_3^0 = \Delta G_{OOH} - \Delta G_O$ :

$$\eta^{\text{OER}} = \max[\Delta G_2^0, \Delta G_3^0]/e - 1.23 \text{ V}. \quad (16)$$

The scaling relations<sup>13</sup> predict a constant adsorption energy difference of  $3.2 \pm 0.2$  eV between the \*OH and \*OOH reaction intermediates on metal and metal-oxide surfaces. The magnitude of the third step can hence be approximated by the magnitude of the second step ( $\Delta G_3^0 = 3.2 \text{ eV} - \Delta G_2^0$ ), which for mechanism **M1** allows us to express the overpotential as a function of the single descriptor  $\Delta G_2^0$

$$\eta_D^{\text{OER}} = \max[\Delta G_2^0, 3.2 \text{ eV} - \Delta G_2^0]/e - 1.23 \text{ V} \quad (17)$$

which for **M1** yields a minimum value of  $0.37 \pm 0.2$  V. We will use the average value of 3.2 eV in our analysis. As will be shown below, we observe deviations from these simplified assumptions for our highly defective surfaces and use these relations primarily to derive the branches of the usual **M1** activity volcano.

## Results & Discussion

### Reaction mechanisms with chemical steps

We first analyze the structures in database 1 to identify chemical reaction steps leading to bonds of reaction intermediates with the surface or with co-adsorbates. The \*OH reaction intermediate binds in almost all cases in bridge and top position on the A and B site respectively (see SI Fig. S1a and c) and does therefore not seem to participate in chemical reaction steps. The \*OOH and \*O intermediates, on the other hand, show three kind of additional bonds as a result of chemical reaction steps: Hydrogen bonds between the \*OOH reaction intermediate and other co-adsorbates such as O (\*OOH-O) or OH (\*OOH-OH),<sup>8,15,17</sup> oxygen dimers involving an \*O reaction intermediate and a lattice oxygen (\*O-O<sub>l</sub>, see SI Fig. S1b

and d) and for the oxynitride also oxygen-nitrogen dimers ( $^*\text{O-N}_l$ ) involving an  $^*\text{O}$  reaction intermediate and a lattice nitrogen. We have previously shown formation of these dimers on oxynitrides to be governed by charge transfer out of the antibonding  $\pi^*$  O-N orbitals, which leads to stronger intra-dimer bonds and hence a stronger bond with the surface.<sup>32</sup> This hints that dimer formation occurs when oxygen adsorbate binding to lattice O is competitive compared to binding to surface transition metal sites, which we will confirm below. Based on their bond length (see SI section S5), the dimers are peroxo or superoxo-like species. As hydrogen-bond energies are small (see SI section S6), we will in the following focus on dimer formation.

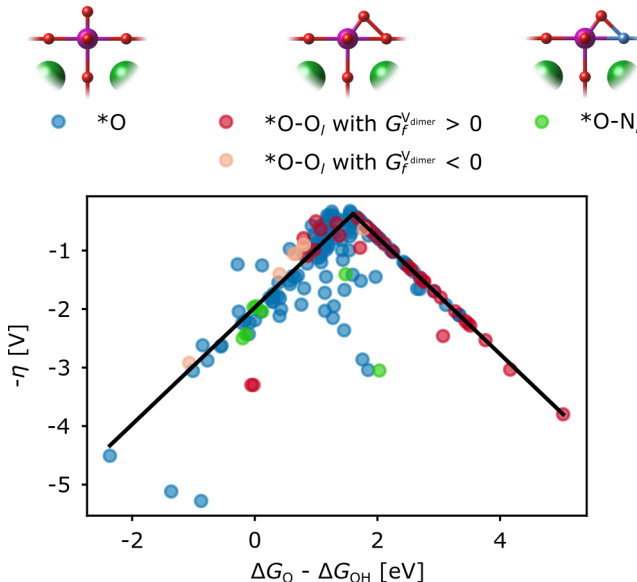


Figure 2: Volcano plot showing the dependence of the thermodynamic overpotential on the single descriptor  $\Delta G_2^0 = \Delta G_{\text{O}} - \Delta G_{\text{OH}}$  for  $\text{LaTiO}_2\text{N}$ ,  $\text{SrRuO}_3$  and  $\text{SrTiO}_3$  of database 1a. The different colors indicate the formation of different types of bonds of the  $^*\text{O}$  reaction intermediate.  $^*\text{O-O}_l$  dimers with positive and negative  $G_f^{\text{V}_{\text{dimer}}}$  are indicated with two different shades of red. The overpotential is calculated according to equations 2-5 and therefore without taking chemical reaction steps into account. Details on the material and defect type associated with each data point can be found in SI section S7.

In Fig. 2 the activity volcano for the conventional reaction mechanism **M1** (and its related mechanism **M4** for the cases where dimer formation occurs) is depicted for database 1a. While most of the data points are close to the overpotential predicted by the single

descriptor  $\eta_D$ , a not insignificant number also deviates from this predicted value. We have shown in previous work<sup>30</sup> that this deviation is related to strong binding of \*OOH adsorbates for oxynitrides, rendering step 4 (\*OOH  $\rightarrow$  O<sub>2</sub>) potential limiting, as a result of which  $\Delta G_2^0$  can no longer be used as a descriptor for the overpotential. We stress that these calculated overpotentials do so far not include chemical steps that could occur due to additional reaction intermediates. We will see in the section on the material dependence that this is a good approximation for **M1**. In Fig. 2 we distinguish the binding configuration of oxygen by different colors, blue data points denoting no dimer formation, dark and light red data points indicating \*O-O<sub>l</sub> dimer formation and green data points standing for \*O-N<sub>l</sub> anion dimer formation (for simplicity also just called “dimers” in the following). We see that \*O-O<sub>l</sub> dimers occur for a wide range ( $-1 \text{ eV} < \Delta G_2^0 < 5 \text{ eV}$ ) of the descriptor, while \*O-N<sub>l</sub> dimer formation occurs only for  $0 \text{ eV} < \Delta G_2^0 < 2 \text{ eV}$ . It is particularly noteworthy that despite the fact that this range includes the top of the volcano, the computed overpotentials in presence of \*O-N<sub>l</sub> dimers are large ( $\eta > 1.5 \text{ eV}$ ), which can be attributed to strong O-N bonds<sup>44</sup> as discussed in more detail below.

Dimers could be involved in different OER reaction mechanisms and we will here consider **M4** and **M3** shown in Fig. 1. To determine whether a dimer can directly evolve as O<sub>2</sub> as required for **M3**, we compute the oxygen vacancy formation energy as a result of dimer desorption  $G_f^{\text{V}_{\text{dimer}}}$  for database 1a:

$$G_f^{\text{V}_{\text{dimer}}} = E_{\text{V}_\text{O}} + E_{\text{O}_2} - E_{\text{dimer}} + (\Delta \text{ZPE} - T \Delta S)_{\text{dimer}} \quad (18)$$

where  $E_{\text{V}_\text{O}}$  is the energy of the slab with the lattice oxygen missing and  $E_{\text{dimer}}$  the energy of the slab with the dimer. Since  $E_{\text{O}_2}$  was determined according to equation 15 this dimer vacancy formation energy corresponds to an oxygen rich environment, which is realistic under OER conditions. We, however, also calculated the dimer vacancy formation energy

within the thermodynamic stability range of the different materials, which is shown in SI section S8. A negative dimer vacancy formation energy indicates that dimer desorption is energetically favorable and mechanism **M3** is feasible, which is highlighted by light red data points in Fig. 2, as opposed to the dark red data points indicating unfavorable dimer vacancy formation. We find that the majority of dimers do not spontaneously evolve as  $O_2$  (see also SI Fig. S14), making mechanism **M4** (O-O coupling but without dimer desorption) energetically more favorable compared to the **M3** lattice oxygen OER mechanism in these cases. Nevertheless there are a number of active sites in database 1a, where mechanism **M3** is feasible. In summary we have shown in this section that chemical  $*O-O_l$  (and on oxynitrides also  $*O-N_l$ ) dimer formation can occur, which, depending on the dimer vacancy formation energy, can lead to the alternative **M3** lattice oxygen OER mechanism.

## Dimer formation energetics

In the previous section, we established that dimer formation could occur, leading to reaction mechanisms **M3** or **M4**, depending on whether these dimers can spontaneously evolve as  $O_2$  or not. From Fig. 2 it is, however, difficult to observe clear trends as to when these different mechanisms are active, which is why in this section, we will further analyze this data.

Attempts to fit various descriptors (see SI section S2 for details) yielded only limited insights. Multidimensional descriptors including geometric and electronic features obtained via the Sure Independent Screening and Sparsifying Operator (SISSO)<sup>45</sup> identified the oxygen  $2p$  band center as the best single descriptor for catalytic activity, an increased descriptor dimension of 2 and a rung 1 yielding small improvements in RMSE, while higher dimensions and rungs lead to overfitting. We also find that dimer formation results in an inverse correlation with the oxygen  $2p$  band center compared to sites without dimer formation that behave in the same way as other oxides.<sup>46</sup>

Apart from these descriptors, we, more importantly, identify in Fig. 3a a clear scaling relation between the OH adsorption energy  $\Delta G_{OH}$  and the adsorption energy for an  $*O$  in

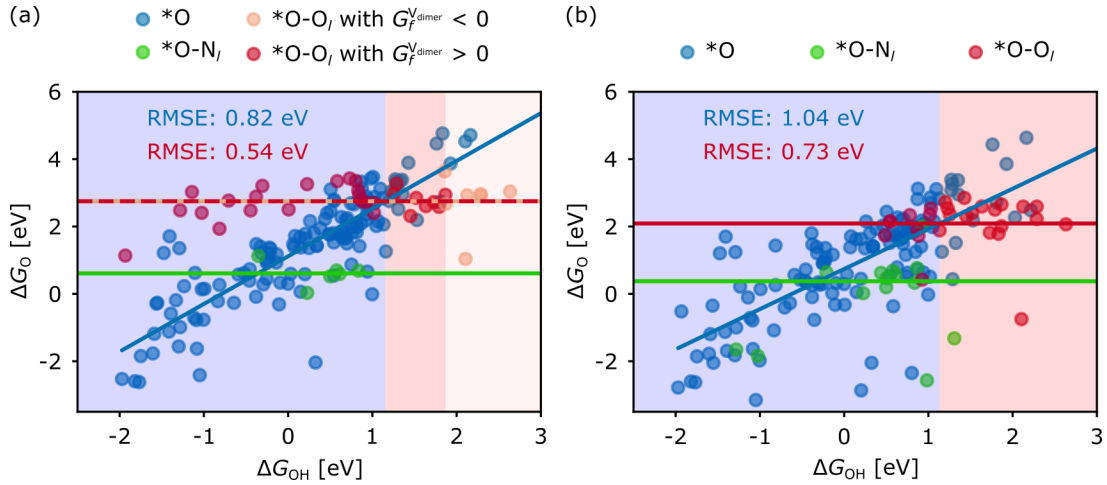


Figure 3:  $\Delta G_O$  as a function of  $\Delta G_{OH}$  for the calculations of (a) database 1a without sampling of different oxygen adsorbate positions and (b) database 1b with sampling of different oxygen adsorbate positions. Oxygen adsorbates that form a bond with the active site  $*$  in top or bridge position are indicated in blue. Oxygen atoms that form a bond with other (lattice) oxygen or nitrogen are indicated in red and green respectively. Oxygen dimers with a negative  $G_f^{V_{dimer}}$  are indicated in light red. The formation energy of the dimer vacancy was not calculated for database 1b. The blue and red background indicates where  $*O$  and  $*O-O_l$  are predicted to be energetically more stable, respectively, while the light and dark red backgrounds distinguish spontaneous and non-spontaneous dimer desorption. Details on the material and defect type associated with each data point can be found in SI section S7.

top or bridge position  $\Delta G_{\text{O}}^{*\text{O}}$  (blue data points). On the other hand, the adsorption energy of  $^*\text{O}$  when it has formed a dimer either with surface oxygen  $\Delta G_{\text{O}}^{*\text{O}-\text{O}_l}$  (light red and dark red data points) or with surface nitrogen  $\Delta G_{\text{O}}^{*\text{O}-\text{N}_l}$  (green data points) does not systematically depend on  $\Delta G_{\text{OH}}$  and we hence fit these with horizontal lines. This broken scaling relation between the OH and dimer O adsorbates is not surprising, since the dimer adsorbs in a completely different configuration, relying on bonds with the B site as well as with lattice oxygen. The vertical difference between the red and blue fitted lines in Fig. 3a indicates the energy difference associated with dimer formation. In the region shaded in blue,  $^*\text{O}$  in top or bridge position is more stable and in the two regions shaded in light/dark red, the  $\text{O}-\text{O}_l$  dimer is more stable.

In Fig. 3a, we observe a number of red data points in the blue shaded area and a number of blue data points in the red shaded area, i.e. where the respectively other  $^*\text{O}$  configuration would be energetically favorable. This observation could be related to an energy barrier preventing the structural optimizer to converge towards the minimum energy state. We confirm this hypothesis by repeating the analysis for database 1b where we sampled different oxygen adsorbate starting positions (see SI section S3 for details). As shown in Fig. 3b we find that most of the unstable data points indeed “fall” towards the fitted line with the lower  $\Delta G_{\text{O}}$ .

The data in Fig. 3 clearly shows that dimer formation is restricted to materials and sites that have a large  $\Delta G_{\text{OH}} > 1$  eV and hence weakly bind OH at the cation site. As shown in SI Figs. S12 and S13, dimer formation most frequently occurs on  $\text{SrTiO}_3$  and  $\text{SrRuO}_3$  surfaces, where the latter need to contain cation vacancies, while the former can also be stoichiometric. For the oxynitride, only very few sites lead to dimer formation. In Fig. 3a we moreover distinguish cases where the dimer vacancy formation is energetically favorable (light red data points,  $G_f^{\text{V}_{\text{dimer}}} < 0$ ) from the ones where it is not favorable (dark red data points,  $G_f^{\text{V}_{\text{dimer}}} > 0$ ). The clustering of the light red data points in the region  $\Delta G_{\text{OH}} > 1.8$  eV (shown by the light red background) indicates that the dimer will spontaneously evolve as

O<sub>2</sub> only on very weakly binding surfaces (see also SI Fig. S14). While we did not calculate  $G_f^{\text{V}_{\text{dimer}}}$  for database 1b (Fig. 3b), we expect similar results. We can thus conclude that for strongly binding surfaces with  $\Delta G_{\text{OH}} < 1$  eV no dimers are formed and mechanisms **M1** or **M2** occur. For intermediate  $\Delta G_{\text{OH}}$  between 1 eV and 1.8 eV dimers are formed but cannot spontaneously evolve as O<sub>2</sub> and mechanism **M4** is active. For  $\Delta G_{\text{OH}} > 1.8$  eV mechanism **M3**, where a dimer is formed and then evolves as O<sub>2</sub>, is most favorable. We note here that the overbinding of O<sub>2</sub> in GGA may also affect the energy gain associated with dimer formation, however to an extent that is not easily quantifiable, given the uncertainty of the dimer charge state (see SI section S5). Assuming the dimer state is at most higher in energy by the O<sub>2</sub> overbinding of 0.79 eV,<sup>47</sup> then \*O-O<sub>l</sub> dimer formation would be restricted to very weakly binding surfaces (i.e. SrTiO<sub>3</sub> and few defective SrRuO<sub>3</sub> configurations, see SI Figs. S12 and S13), while \*O-N<sub>l</sub> dimers on oxynitrides are more prevalent.

Since the vertical energy difference between the red and blue fitted lines in Fig. 3 corresponds to the dimer formation energy (reaction step 4.2 in Fig. 1e), this implies that when **M3** is active, dimer formation is always associated with an energy lowering of more than 1 eV relative to an upright O adsorbate. For the region where **M4** is active, on the other hand, the same energy lowering is always smaller than 1 eV. These results rationalize previous theoretical studies that showed lattice OER to preferentially occur on surfaces with weak adsorption strength and facile vacancy formation.<sup>25,28</sup>

For \*O-N<sub>l</sub> dimers formed on the oxynitride, we also find an almost constant adsorption energy, which is approximately 2 eV lower than the one for \*O-O<sub>l</sub> (see Fig. 3). We note that since not all surfaces contain nitrogen, we do not observe all data points to “fall” down to the \*O-N<sub>l</sub> line in Fig. 3b for the region where we predict \*O-N<sub>l</sub> to be most stable ( $\Delta G_{\text{OH}} > -0.3$  eV). Nevertheless by considering only the subset of N containing surfaces, this trend can be recovered (not shown). The constant energy difference of  $\Delta G_{\text{O}}^{*\text{O}-\text{O}_l}$  and  $\Delta G_{\text{O}}^{*\text{N}-\text{O}_l}$  implies that \*O-N<sub>l</sub> dimers already form on surfaces with stronger OH adsorption and that \*O-N<sub>l</sub> dimer formation corresponds to a significantly more exothermic chemical step compared to \*O-O<sub>l</sub>



dimer formation. This suggests that very stable dimer O-N bonds could be at the origin of high overpotentials computed in Fig. 2 and thus the low catalytic activity of oxynitrides.

## Implications of chemical steps on the thermodynamic overpotential

We continue by investigating how additional reaction intermediates and the resulting chemical steps in a computational analysis affect the predicted thermodynamic overpotential. We focus in particular on the mechanism **M3** and dimer formation, which we have established above to be exothermic in excess of 1 eV for materials and sites, where a negative  $G_f^{V_{\text{dimer}}}$  enables **M3**, such as SrTiO<sub>3</sub> and cation deficient SrRuO<sub>3</sub>. So far the exothermic nature of chemical steps was only considered as a requirement for the kinetic feasibility of **M3**, without considering their effect on the overpotential.<sup>29</sup>

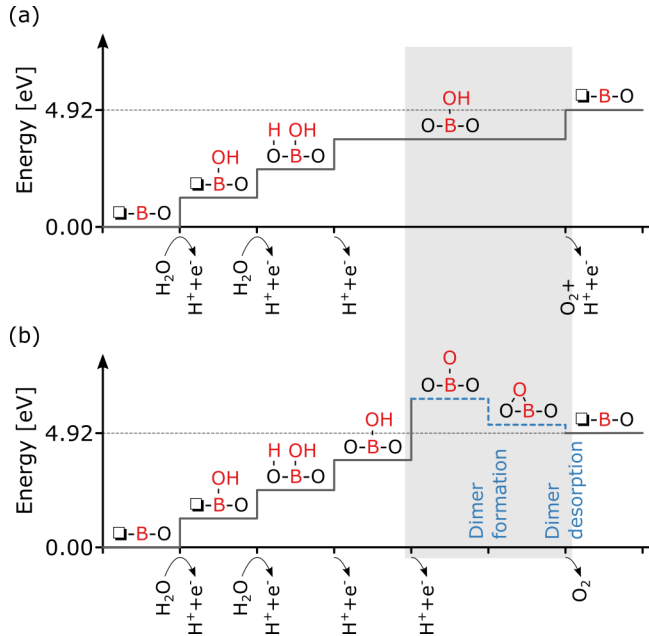


Figure 4: Schematic free energy diagram for reaction mechanism **M3** at 0 V vs. RHE (a) without taking chemical steps into considerations and (b) taking them into considerations via additional reaction intermediates. Chemical steps are indicated by dashed blue and electrochemical steps by solid black lines. The background shading indicates where the free energy profiles differ.

For highly active reaction mechanisms, chemical steps should not only be exothermic (or slightly endothermic such that they can still be overcome by temperature or other reaction

conditions), but their associated free energy gain should also be as small as possible. This is due to the fact that any decrease in energy caused by an exothermic chemical step will have to be compensated by an increase in height of the electrochemical steps to maintain the overall free energy difference of 4.92 eV for one OER cycle. This point is schematically shown in Fig. 4, where we compare **M3** without and with dimer formation and desorption chemical steps. In panel (a), we assume, for simplicity, that all four electrochemical steps have the same magnitude. In panel (b), by the Bell-Evans-Polyani principle,<sup>48,49</sup> we make the reasonable assumption that the highly exothermic dimer formation has a small or vanishing barrier, implying that the dimer will form more rapidly after \*OH deprotonation than a direct desorption of O<sub>2</sub> could occur. We note, however, that the high-energy \*O state could be (partially) circumvented if deprotonation and dimer formation occur in a concerted fashion.

The first three electrochemical steps are identical in panels (a) and (b) and consequently have the same magnitude. Given that the total free energy difference of 4.92 eV needs to be maintained for one OER cycle also in panel (b), implies that the intermediate following the fourth step (B-OH  $\rightarrow$  B-O) needs to increase by the magnitude of the exothermic chemical steps. This step is consequently larger than the others and becomes potential limiting, leading to a larger thermodynamic overpotential than the one obtained by neglecting exothermic chemical steps in panel (a). Neglecting the chemical steps, as in panel (a) thus leads to an underestimation of the overpotential.

For dimer formation in **M3**, we know the chemical step to be exothermic in excess of 1 eV when  $G_f^{V_{\text{dimer}}} < 0$  and **M3** is active. We can hence obtain a rough estimate of the increase in overpotential for the idealized case, depicted in Fig. 4. Whereas in panel (a) all steps are of equal magnitude 1.23 eV, in panel (b) the potential limiting step is 1.23 eV + 1 eV, leading to an overpotential of 1 eV. We note that this estimation is for an ideal catalyst and that scaling relations between the adsorption energies of the intermediates may affect the change in overpotential. We will show such a real case for the material SrFeO<sub>3</sub> in the next section.

The above considerations, while derived for dimer formation in **M3**, are general and

independent of the reaction mechanism. Exothermic chemical steps will hence generally increase the overpotential. Endothermic chemical steps will have the opposite effect and decrease the overpotential, but at the same time negatively affect the reaction kinetics and require higher temperature. As such, endothermic chemical steps affect the kinetics, while exothermic chemical steps can affect the thermodynamic overpotential.

Based on these considerations we propose that other reaction mechanisms without exothermic chemical reaction steps are likely to become more favorable than mechanisms such as **M3** that include exothermic chemical steps in excess of 1 eV. One possible competing mechanism is **M1** that, as we will show in the next section, does not include significant exothermic chemical reaction steps. Similarly, also for the conventional reaction mechanism on a lattice oxygen vacancy **M2**, we would expect chemical steps not to play a significant role. Based on the data developed in the previous section, we can further conclude that for **M4** the chemical steps are less important than for **M3** as the energy difference between  $\Delta G_{\text{O}}^{*\text{O}}$  and  $\Delta G_{\text{O}}^{*\text{O}-\text{O}_l}$  is smaller than 1 eV when the dimer does not spontaneously evolve as  $\text{O}_2$ . It is however important to note, that an energy lowering through a chemical reaction step only has implications on the overpotential if it increases the largest electrochemical step. Therefore, each mechanism has to be carefully analyzed, a point we will briefly return to in the next section.

We also note here that the choice of reaction intermediates and therefore the considered chemical steps can be somewhat arbitrary. As such, mechanism **M3** is the same as previously investigated<sup>25,28,29</sup> but we combined the electrochemical and chemical steps differently, resulting in a reaction scheme that is not completely identical. Moreover one of these studies included additional reaction intermediates and associated chemical reaction steps.<sup>29</sup> Based on the above discussion we can say that while determining the energetic magnitude of chemical substeps is crucial, their exact location in a reaction step will not affect their effect on the electrochemical steps. As such, including additional reaction intermediates will not change the conclusions of the present work.

## Material dependence of M3 and M4

Finally, we will analyze dimer formation and desorption for perfectly stoichiometric (001) surfaces of eight different perovskite oxides and oxynitrides ( $\text{LaTiO}_2\text{N}$ ,  $\text{SrTiO}_3$ ,  $\text{SrRuO}_3$ ,  $\text{NaTaO}_3$ ,  $\text{NaNbO}_3$ ,  $\text{LaFeO}_3$ ,  $\text{SrFeO}_3$  and  $\text{LaMnO}_3$ ) contained in database 2. This set extends the one of database 1 by different +1/+5, +2/+4 and +3/+3 perovskite oxides that are known photo- or electrocatalysts. This will give us the possibility to evaluate the trends observed for defective  $\text{SrTiO}_3$ ,  $\text{LaTiO}_2\text{N}$  and  $\text{SrRuO}_3$  for a larger variety of materials and to investigate trends in binding energies without the noise associated with the structural flexibility of defective surfaces.

We first use the results for these additional materials to rationalize why the conventional reaction mechanisms **M1** has been successfully used to predict the catalytic activity for different materials without considering chemical reaction steps.<sup>13</sup> We restrict ourselves to the B terminated surface as it is thermodynamically more stable and was predominantly used for computational overpotential predictions of perovskite oxides.<sup>50</sup> By explicitly considering the intermediate  $^*\text{OO}$  and the desorption step shown in equation 7 we determine the energy difference of this chemical step  $\Delta G^{*+\text{O}_2} - \Delta G^{*\text{OO}}$  to range from slightly exothermic (-0.1 eV for  $\text{LaTiO}_2\text{N}$  and  $\text{SrTiO}_3$ ) to highly endothermic (1.2 eV for  $\text{NaNbO}_3$  and  $\text{SrRuO}_3$ ) (see SI section S9 for more details). A slightly exothermic step involving  $^*\text{OO}$  will not affect the thermodynamic overpotential of **M1** as the final step (equation 5) is normally not the limiting step and is unlikely to become so with an increase of only 0.1 eV. An endothermic chemical step would actually decrease the height of the final electrochemical step of **M1**, however also without affecting the overpotential since the final step is rarely limiting. However, in this case the (large) endothermic chemical step needs to be overcome by an increased temperature. This implies that the electrochemical steps of **M1** are fairly insensitive to possible chemical steps.

To analyze the feasibility of the alternative mechanisms, we show, analogous to Fig. 3, in Fig. 5a  $\Delta G_{\text{O}}$  for the oxygen dimer ( $^*\text{O}-\text{O}_l$ ) as well as oxygen in the top or bridge position

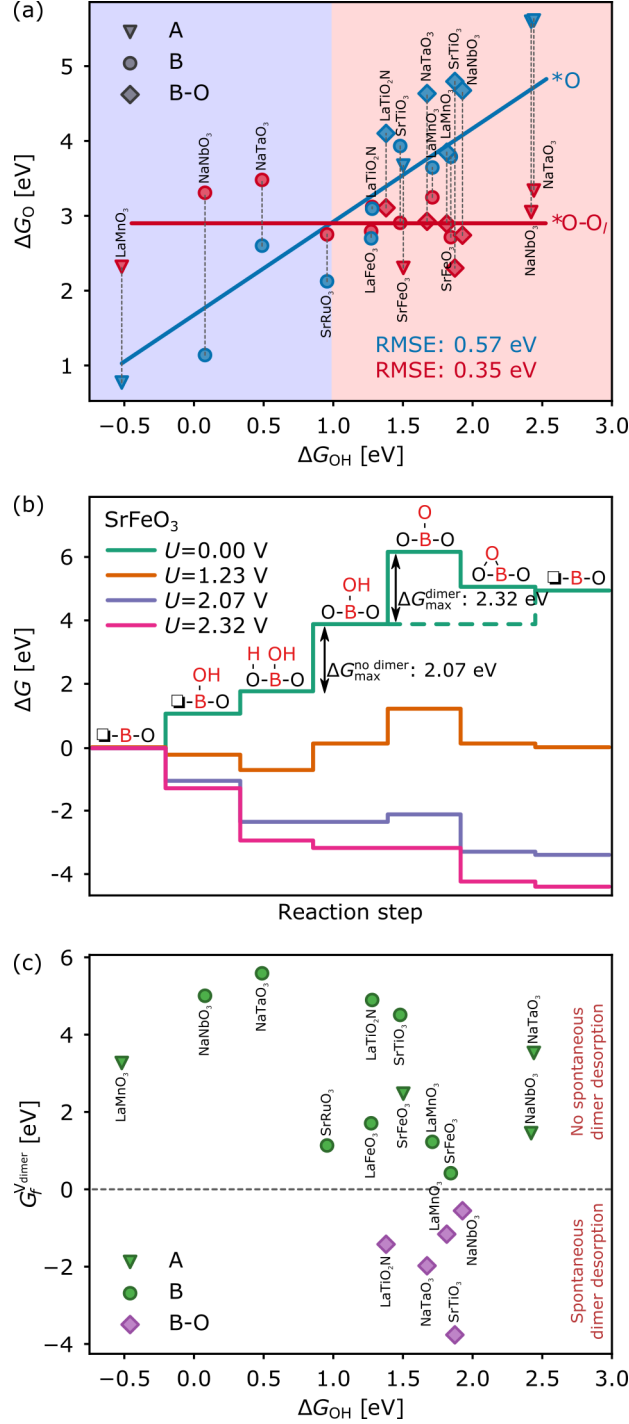


Figure 5: (a) Oxygen adsorption energy  $\Delta G_O$  in bridge and top position (blue data points) as well as a dimer (red data points) as a function of  $\Delta G_{OH}$  on stoichiometric A (triangles), B (circles) and B-O (diamonds) terminated (001) surfaces of 8 different perovskite materials in database 2. Dashed vertical lines indicate point pairs. (b) Free energy diagrams for mechanism **M3** including dimer formation as shown in Fig. 4b for  $\text{SrFeO}_3$  at different potentials. (c) Dimer vacancy formation energy  $G_f^{V_{\text{dimer}}}$  on clean A (triangles), B (circles) and O-covered B (diamonds) terminated surfaces of the materials in database 2.

(\*O) for the A and B terminated surfaces respectively. As expected, we find a good correlation between  $\Delta G_{\text{OH}}$  and  $\Delta G_{\text{O}}^{*\text{O}}$ , with significantly less scatter than for database 1. Further, like for database 1,  $G_{\text{O}}^{*\text{O}-\text{O}_l}$  is fairly insensitive on  $\Delta G_{\text{OH}}$ . These same correlations imply that the above conclusions derived from database 1 apply also to the additional materials of database 2 listed in Fig. 5 and that dimer formation generally occurs for weakly binding surfaces with  $\Delta G_{\text{OH}} > 1$  eV, resulting in a reaction mechanism such as **M3** or **M4**, while for more strongly binding materials ( $\Delta G_{\text{OH}} < 1$ ) mechanisms such as **M1** or **M2** are active. We note that while dimer formation is favorable for few A and B-terminated surfaces, it is favorable for all B-O terminated surfaces, that are often relevant under OER conditions.<sup>51</sup> We note, however, that surface Pourbaix diagrams showing this were not constructed in the present work. This energy difference between \*O and \*O—O<sub>l</sub> can, with increasing  $\Delta G_{\text{OH}}$ , lead to large chemical steps that will have to be compensated by the electrochemical steps and may lead to higher thermodynamic overpotentials. This is illustrated in Fig. 5b for SrFeO<sub>3</sub>, where dimer formation is exothermic and **M3** with the extra steps shown in Fig. 4b is favorable. Without dimer formation, the highest step amounts to 2.07 eV. Adding the exothermic dimer formation and desorption chemical steps changes the potential limiting electrochemical step that now has a magnitude of 2.32 eV. The effect of this change in potential limiting step is shown by the free energy profiles at higher voltages, where the chemical steps maintain their height, while at 2.07 V one of the electrochemical steps remains uphill and only vanishes at 2.32 V. Considering chemical steps hence increases the overpotential by 0.25 V for SrFeO<sub>3</sub>.

In Fig. 5c we show  $G_f^{\text{V}_{\text{dimer}}}$  as a function of  $\Delta G_{\text{OH}}$  for the same eight perovskite materials. There is no clear correlation between  $\Delta G_{\text{OH}}$  and the dimer vacancy formation energy, contrary to what was observed for database 1. This result implies that  $G_f^{\text{V}_{\text{dimer}}}$  depends on factors other than  $\Delta G_{\text{OH}}$  and that, as previously suggested,  $\Delta G_{\text{OH}}$  can at most be used as a descriptor for vacancy formation for the same material or a certain material family, such as B terminated surfaces with the same A-site.<sup>25</sup> Nevertheless we find that oxygen-covered

B-terminated surfaces generally show exothermic  $G_f^{V_{\text{dimer}}}$ , while clean A or B terminated surfaces have endothermic  $G_f^{V_{\text{dimer}}}$ , which is due to the fact that oxygen vacancies can be spontaneously filled by nearby oxygen co-adsorbates, lowering  $G_f^{V_{\text{dimer}}}$ . This process has previously been reported for  $\text{SrCoO}_3$  and  $\text{SrTaO}_2\text{N}$ , where lattice oxygen vacancies were healed by oxygen co-adsorbates.<sup>31,52</sup>

Overall the results for database 2 imply that while dimer formation and hence the occurrence of either mechanism **M3** or **M4** is general for materials that weakly bind OH, the spontaneous evolution of  $\text{O}_2$  that enables **M3** depends on other factors and needs to be evaluated for each material.

## Conclusions

We have evaluated the effect of additional reaction intermediates with resulting chemical steps in a computational analysis of previously proposed OER mechanisms. Based on DFT calculations for defective as well as stoichiometric surfaces of different perovskite oxides and oxynitrides, our results show that exothermic chemical steps such as oxygen dimer formation ( $*\text{O} \rightarrow *\text{O}-\text{O}_l$ ) can affect the calculated thermodynamic overpotential and thus the feasibility of a reaction mechanism. This is rooted in the energy lowering due to exothermic chemical reaction steps that needs to be compensated by an equivalent increase in magnitude of the electrochemical steps.

We have shown this to be the case for a mechanism that was previously proposed to have a low overpotential on weakly binding perovskites, however without considering the effect of chemical steps on the overpotential. Our results highlight that when this mechanism is enabled by spontaneous  $*\text{O}-\text{O}_l$  desorption, the  $*\text{O}$  adsorbate adopts a bidentate bridged  $*\text{O}-\text{O}_l$  dimer structure, with an exothermic chemical step of at least 1 eV. This chemical step may increase the overpotential by up to the same amount and can shift the most favorable reaction pathway to other mechanisms, such as the conventional OER mechanism with  $*\text{OH}$ ,

\*O and \*OOH intermediates, the overpotential of which we show not to be generally affected by chemical steps.

We find oxygen dimer formation to be particularly relevant on perovskite surfaces with weak binding at the cation sites. This can be rationalized by weakly material-dependent O-O<sub>l</sub> bond strengths, while metal-O bond strengths strongly depend on the metal element. As such dimer formation and thus exothermic chemical steps occur when O-O<sub>l</sub> bonds become competitive with weak metal-O bonds.

Our findings are, however, not limited to oxygen dimer formation but more generally show that exothermic chemical steps can affect the thermodynamic overpotential. This implies that additional reaction intermediates leading to chemical steps need to be crucially included when computationally evaluating alternative OER reaction mechanisms. While explicitly considering exothermic chemical steps should generally increase overpotentials, each reaction mechanism has to be analyzed in detail as the chemical steps may affect electrochemical steps other than the largest potential limiting one.

## Supporting Information Available

Additional computational details, descriptor search results, characterization of dimer and hydrogen bonds and results related to dimer-vacancy formation.

## Acknowledgement

This research was funded by the SNF Professorship Grants PP00P2\_157615, PP00P2\_187185 and an associated mobility grant.

Calculations were performed on UBELIX (<http://www.id.unibe.ch/hpc>), the HPC cluster at the University of Bern, the Swiss National Supercomputing Centre (CSCS) under project s766 and SuperMUC at GCS@LRZ, Germany, for which we acknowledge PRACE for awarding us access. We would also like to thank Runhai Ouyang for helpful discussions related to



SISSO.

## References

- (1) Montoya, J. H.; Seitz, L. C.; Chakthranont, P.; Vojvodic, A.; Jaramillo, T. F.; Nørskov, J. K. Materials for solar fuels and chemicals. Nat. Mater. **2017**, 16, 70–81.
- (2) Hong, W. T.; Risch, M.; Stoerzinger, K. A.; Grimaud, A.; Suntivich, J.; Shao-Horn, Y. Toward the rational design of non-precious transition metal oxides for oxygen electrocatalysis. Energy Environ. Sci. **2015**, 8, 1404–1427.
- (3) Hwang, J.; Rao, R. R.; Giordano, L.; Katayama, Y.; Yu, Y.; Shao-Horn, Y. Perovskites in catalysis and electrocatalysis. Science **2017**, 358, 751–756.
- (4) Koper, M. T. Thermodynamic theory of multi-electron transfer reactions: Implications for electrocatalysis. J. Electroanal. Chem. **2011**, 660, 254–260.
- (5) Hessels, J.; Detz, R. J.; Koper, M. T. M.; Reek, J. N. H. Rational design rules for molecular water oxidation catalysts based on scaling relationships. Chem. – Eur. J. **2017**, 23, 16413–16418.
- (6) Craig, M. J.; Coulter, G.; Dolan, E.; Soriano-López, J.; Mates-Torres, E.; Schmitt, W.; García-Melchor, M. Universal scaling relations for the rational design of molecular water oxidation catalysts with near-zero overpotential. Nat. Commun. **2019**, 10, 4993.
- (7) Weder, N.; Probst, B.; Sévery, L.; Fernández-Terán, R. J.; Beckord, J.; Blacque, O.; Tilley, S. D.; Hamm, P.; Osterwalder, J.; Alberto, R. Mechanistic insights into photocatalysis and over two days of stable H<sub>2</sub> generation in electrocatalysis by a molecular cobalt catalyst immobilized on TiO<sub>2</sub>. Catal. Sci. Technol. **2020**, 10, 2549–2560.
- (8) Ping, Y.; Nielsen, R. J.; Goddard, W. A. The reaction mechanism with free energy

- barriers at constant potentials for the oxygen evolution reaction at the IrO<sub>2</sub> (110) surface. J. Am. Chem. Soc. **2017**, 139, 149–155.
- (9) Huang, Z.-F.; Song, J.; Du, Y.; Xi, S.; Dou, S.; Nsanzimana, J. M. V.; Wang, C.; Xu, Z. J.; Wang, X. Chemical and structural origin of lattice oxygen oxidation in Co–Zn oxyhydroxide oxygen evolution electrocatalysts. Nat. Energy **2019**, 4, 329–338.
- (10) Pan, Y.; Xu, X.; Zhong, Y.; Ge, L.; Chen, Y.; Veder, J.-P. M.; Guan, D.; O’Hayre, R.; Li, M.; Wang, G.; Wang, H.; Zhou, W.; Shao, Z. Direct evidence of boosted oxygen evolution over perovskite by enhanced lattice oxygen participation. Nat. Commun. **2020**, 11, 2002.
- (11) Liu, J.; Jia, E.; Stoerzinger, K. A.; Wang, L.; Wang, Y.; Yang, Z.; Shen, D.; Engelhard, M. H.; Bowden, M. E.; Zhu, Z.; Chambers, S. A.; Du, Y. Dynamic lattice oxygen participation on perovskite LaNiO<sub>3</sub> during oxygen evolution reaction. J. Phys. Chem. C **2020**, 124, 15386–15390.
- (12) Ferreira de Araújo, J.; Dionigi, F.; Merzdorf, T.; Oh, H.-S.; Strasser, P. Evidence of Mars-Van-Krevelen mechanism in the electrochemical oxygen evolution on Ni-based catalysts. Angew. Chem., Int. Ed. **2021**, 60, 14981–14988.
- (13) Man, I. C.; Su, H.-Y.; Calle-Vallejo, F.; Hansen, H. A.; Martínez, J. I.; Inoglu, N. G.; Kitchin, J.; Jaramillo, T. F.; Nørskov, J. K.; Rossmeisl, J. Universality in oxygen evolution electrocatalysis on oxide surfaces. ChemCatChem **2011**, 3, 1159–1165.
- (14) Rossmeisl, J.; Qu, Z.-W.; Zhu, H.; Kroes, G.-J.; Nørskov, J. K. Electrolysis of water on oxide surfaces. J. Electroanal. Chem. **2007**, 607, 83–89.
- (15) Rao, R. R.; Kolb, M. J.; Halck, N. B.; Pedersen, A. F.; Mehta, A.; You, H.; Stoerzinger, K. A.; Feng, Z.; Hansen, H. A.; Zhou, H.; Giordano, L.; Rossmeisl, J.; Vegge, T.; Chorkendorff, I.; Stephens, I. E. L.; Shao-Horn, Y. Towards identifying the

- active sites on RuO<sub>2</sub>(110) in catalyzing oxygen evolution. Energy Environ. Sci. **2017**, 10, 2626–2637.
- (16) Pavlovic, Z.; Ranjan, C.; van Gastel, M.; Schlögl, R. The active site for the water oxidising anodic iridium oxide probed through in situ Raman spectroscopy. Chem. Commun. **2017**, 53, 12414–12417.
- (17) Rao, R. R.; Kolb, M. J.; Giordano, L.; Pedersen, A. F.; Katayama, Y.; Hwang, J.; Mehta, A.; You, H.; Lunger, J. R.; Zhou, H.; Halck, N. B.; Vegge, T.; Chorkendorff, I.; Stephens, I. E. L.; Shao-Horn, Y. Operando identification of site-dependent water oxidation activity on ruthenium dioxide single-crystal surfaces. Nat. Catal. **2020**, 3, 516–525.
- (18) Lee, Y.-L.; Gadre, M. J.; Shao-Horn, Y.; Morgan, D. Ab initio GGA+U study of oxygen evolution and oxygen reduction electrocatalysis on the (001) surfaces of lanthanum transition metal perovskites LaBO<sub>3</sub> (B= Cr, Mn, Fe, Co and Ni. Phys. Chem. Chem. Phys. **2015**, 17, 21643–21663.
- (19) Montoya, J. H.; Doyle, A. D.; Nørskov, J. K.; Vojvodic, A. Trends in adsorption of electrocatalytic water splitting intermediates on cubic ABO<sub>3</sub> oxides. Phys. Chem. Chem. Phys. **2018**, 20, 3813–3818.
- (20) Rossmeisl, J.; Logadottir, A.; Nørskov, J. K. Electrolysis of water on (oxidized) metal surfaces. Chem. Phys. **2005**, 319, 178–184.
- (21) Valdés, Á.; Qu, Z.-W.; Kroes, G.-J.; Rossmeisl, J.; Nørskov, J. K. Oxidation and photo-oxidation of water on TiO<sub>2</sub> surface. J. Phys. Chem. C **2008**, 112, 9872–9879.
- (22) Mom, R. V.; Cheng, J.; Koper, M. T. M.; Sprik, M. Modeling the oxygen evolution reaction on metal oxides: The influence of unrestricted DFT calculations. J. Phys. Chem. C **2014**, 118, 4095–4102.

- (23) Sundararaman, R.; III, W. A. G.; Arias, T. A. Grand canonical electronic density-functional theory: Algorithms and applications to electrochemistry. J. Chem. Phys. **2017**, 146, 114104 15.
- (24) Dickens, C. F.; Kirk, C.; Nørskov, J. K. Insights into the electrochemical oxygen evolution reaction with ab initio calculations and microkinetic modeling: Beyond the limiting potential volcano. J. Phys. Chem. C **2019**, 123, 18960–18977.
- (25) Rong, X.; Parolin, J.; Kolpak, A. M. A fundamental relationship between reaction mechanism and stability in metal oxide catalysts for oxygen evolution. ACS Catal. **2016**, 6, 1153–1158.
- (26) Ahmed, M.; Xinxin, G. A review of metal oxynitrides for photocatalysis. Inorg. Chem. Front. **2016**, 3, 578–590.
- (27) Grimaud, A.; Diaz-Morales, O.; Han, B.; Hong, W. T.; Lee, Y.-L.; Giordano, L.; Storerzinger, K. A.; Koper, M. T.; Shao-Horn, Y. Activating lattice oxygen redox reactions in metal oxides to catalyse oxygen evolution. Nat. Chem. **2017**, 9, 457.
- (28) Yoo, J. S.; Rong, X.; Liu, Y.; Kolpak, A. M. Role of lattice oxygen participation in understanding trends in the oxygen evolution reaction on perovskites. ACS Catal. **2018**, 8, 4628–4636.
- (29) Yoo, J. S.; Liu, Y.; Rong, X.; Kolpak, A. M. Electronic origin and kinetic feasibility of the lattice oxygen participation during the oxygen evolution reaction on perovskites. J. Phys. Chem. Lett. **2018**, 9, 1473–1479.
- (30) Vonrüti, N.; Aschauer, U. The role of metastability in enhancing water-oxidation activity. Phys. Chem. Chem. Phys. **2019**, 21, 24354–24360.
- (31) Ouhbi, H.; Aschauer, U. Nitrogen loss and oxygen evolution reaction activity of perovskite oxynitrides. ACS Mater. Lett. **2019**, 1, 52–57.

- (32) Bouri, M.; Aschauer, U. Suitability of different  $\text{Sr}_2\text{TaO}_3\text{N}$  surface orientations for photocatalytic water oxidation. Chem. Mater. **2019**, 32, 75–84.
- (33) Rao, R. R.; Kolb, M. J.; Giordano, L.; Pedersen, A. F.; Katayama, Y.; Hwang, J.; Mehta, A.; You, H.; Lunger, J. R.; Zhou, H.; Halck, N. B.; Vegge, T.; Chorkendorff, I.; Stephens, I. E. L.; Shao-Horn, Y. Operando identification of site-dependent water oxidation activity on ruthenium dioxide single-crystal surfaces. Nat. Catal. **2020**, 3, 516–525.
- (34) Vandichel, M.; Busch, M.; Laasonen, K. Oxygen evolution on metal-oxy-hydroxides: Beneficial role of mixing Fe, Co, Ni, explained via bifunctional edge/acceptor route. ChemCatChem **2020**, 12, 1436–1442.
- (35) Giannozzi, P.; Baroni, S.; Bonini, N.; Calandra, M.; Car, R.; Cavazzoni, C.; Ceresoli, D.; Chiarotti, G. L.; Cococcioni, M.; Dabo, I.; Corso, A. D.; de Gironcoli, S.; Fabris, S.; Fratesi, G.; Gebauer, R.; Gerstmann, U.; Gougoussis, C.; Kokalj, A.; Lazzeri, M.; Martin-Samos, L.; Marzari, N.; Mauri, F.; Mazzarello, R.; Paolini, S.; Pasquarello, A.; Paulatto, L.; Sbraccia, C.; Scandolo, S.; Sclauzero, G.; Seitsonen, A. P.; Smogunov, A.; Umari, P.; Wentzcovitch, R. M. Quantum ESPRESSO: a modular and open-source software project for quantum simulations of materials. J. Phys.: Condens. Matter **2009**, 21, 395502.
- (36) Giannozzi, P.; Andreussi, O.; Brumme, T.; Bunau, O.; Buongiorno Nardelli, M.; Calandra, M.; Car, R.; Cavazzoni, C.; Ceresoli, D.; Cococcioni, M.; Colonna, N.; Carnimeo, I.; Dal Corso, A.; De Gironcoli, S.; Delugas, P.; Distasio, R. A.; Ferretti, A.; Floris, A.; Fratesi, G.; Fugallo, G.; Gebauer, R.; Gerstmann, U.; Giustino, F.; Gorni, T.; Jia, J.; Kawamura, M.; Ko, H. Y.; Kokalj, A.; Küçükbenli, E.; Lazzeri, M.; Marsili, M.; Marzari, N.; Mauri, F.; Nguyen, N. L.; Nguyen, H. V.; Otero-De-La-Roza, A.; Paulatto, L.; Poncé, S.; Rocca, D.; Sabatini, R.; Santra, B.; Schlipf, M.; Seitsonen, A. P.; Smogunov, A.; Timrov, I.; Thonhauser, T.; Umari, P.; Vast, N.; Wu, X.; Baroni, S.

- Advanced capabilities for materials modelling with Quantum ESPRESSO. J. Phys.: Condens. Matter **2017**, 29, 465901.
- (37) Perdew, J. P.; Burke, K.; Ernzerhof, M. Generalized gradient approximation made simple. Phys. Rev. Lett. **1996**, 77, 3865.
- (38) Anisimov, V. I.; Zaanen, J.; Andersen, O. K. Band theory and Mott insulators: Hubbard U instead of Stoner I. Phys. Rev. B **1991**, 44, 943.
- (39) Timrov, I.; Marzari, N.; Cococcioni, M. Hubbard parameters from density-functional perturbation theory. Phys. Rev. B **2018**, 98, 085127.
- (40) Bengtsson, L. Dipole correction for surface supercell calculations. Phys. Rev. B **1999**, 59, 12301.
- (41) Nørskov, J. K.; Rossmeisl, J.; Logadottir, A.; Lindqvist, L.; Kitchin, J. R.; Bligaard, T.; Jonsson, H. Origin of the overpotential for oxygen reduction at a fuel-cell cathode. J. Phys. Chem. B **2004**, 108, 17886–17892.
- (42) Sargeant, E.; Illas, F.; Rodríguez, P.; Calle-Vallejo, F. Importance of the gas-phase error correction for O<sub>2</sub> when using DFT to model the oxygen reduction and evolution reactions. J. Electroanal. Chem. **2021**, 896, 115178.
- (43) Gao, D.; Zhou, H.; Cai, F.; Wang, D.; Hu, Y.; Jiang, B.; Cai, W.-B.; Chen, X.; Si, R.; Yang, F.; Miao, S.; Wang, J.; Wang, G.; Bao, X. Switchable CO<sub>2</sub> electroreduction via engineering active phases of Pd nanoparticles. Nano Res. **2017**, 10, 2181–2191.
- (44) Benson, S. W. III - Bond energies. J. Chem. Educ. **1965**, 42, 502.
- (45) Ouyang, R.; Curtarolo, S.; Ahmetcik, E.; Scheffler, M.; Ghiringhelli, L. M. SISSO: A compressed-sensing method for identifying the best low-dimensional descriptor in an immensity of offered candidates. Phys. Rev. Mater. **2018**, 2, 083802.

- (46) Dickens, C. F.; Montoya, J. H.; Kulkarni, A. R.; Bajdich, M.; Nørskov, J. K. An electronic structure descriptor for oxygen reactivity at metal and metal-oxide surfaces. Surf. Sci. **2019**, 681, 122–129.
- (47) Wang, L.; Maxisch, T.; Ceder, G. Oxidation energies of transition metal oxides within the GGA+U framework. Phys. Rev. B **2006**, 73, 195107.
- (48) Bell, R. P. The theory of reactions involving proton transfers. Proc. R. Soc. London, Ser. A **1936**, 154, 414–429.
- (49) Evans, M. G.; Polanyi, M. Inertia and driving force of chemical reactions. Trans. Faraday Soc. **1938**, 34, 11.
- (50) Peña, M.; Fierro, J. Chemical structures and performance of perovskite oxides. Chem. Rev. (Washington, DC, U. S.) **2001**, 101, 1981–2018.
- (51) Raman, A. S.; Patel, R.; Vojvodic, A. Surface stability of perovskite oxides under OER operating conditions: a first principles approach. Faraday Discuss. **2021**, 229, 75–88.
- (52) Tahini, H. A.; Tan, X.; Schwingenschlögl, U.; Smith, S. C. In operando self-healing of perovskite electrocatalysts: A case study of SrCoO<sub>3</sub> for the oxygen evolution reaction. Part. Part. Syst. Charact. **2017**, 34, 1600280.

# TOC Graphic

